consistent with the hypothesis that a combination of plowing and oxidation of the fast cycling carbon pool are the cause of the downward shift in $^{14}C/C$ ratios observed for agricultural soil. To test this hypothesis, we considered what would happen if a native New Zealand soil was mixed to a depth of 20 cm and 25% of the carbon was oxidized (Fig. 2). Through mixing with underlying material, the $^{14}C/C$ ratio for the upper 10 cm of soil was reduced from a native value of 1.08 to 1.02 and the soil carbon inventory in this layer was reduced from 0.26 to 0.22 g/cm^2. We assumed that the increased oxidation took place in the fast cycling pool with an e-folding time of 25 years, eventually removing 25% of the soil's carbon. As a result, after a few decades, the $^{14}C/C$ ratio in the upper 10 cm of the soil dropped to 0.94 and the bulk carbon to 0.16 g/cm^2. The predicted $^{14}C/C$ ratio of 0.94 agrees with the observed average value for cultivated soil collected in 1975.

In summary, the observation that the $^{14}C/C$ ratios for agricultural soil are lower than those for native soils is consistent with a reduction in the amount of humus stored in these soils. Part, but not all, of the radiocarbon reduction can be attributed to preferential oxidation of humus in the fast cycling pool relative to that in the slow cycling pool. These observations suggest that as much as 60 GtC (10 years of fossil fuel CO_2 production at the current rates) could be sequestered if agricultural soil across the globe could be engineered back to its original carbon content.

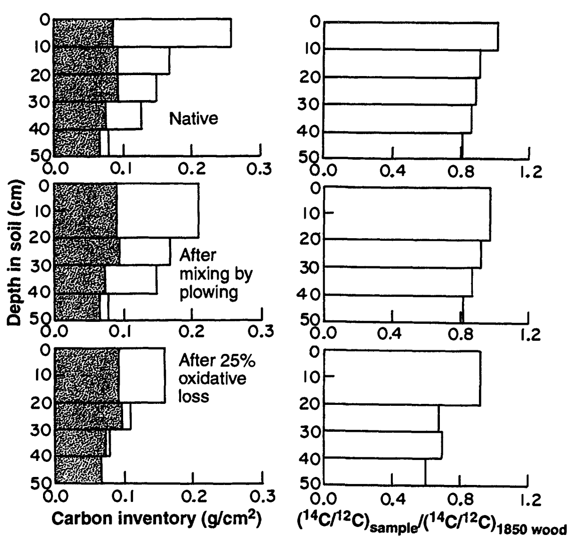

Fig. 2. Hypothetical evolution of native New Zealand soil carbon and radiocarbon subject to changing land use. The top figures illustrate the native radiocarbon ratios and carbon inventories, both of which decrease with depth (*6*). Also shown is the partitioning between fast turnover (unshaded region) and slow turnover (shaded region) carbon pools. The fast pool has a $^{14}C/C$ ratio of 1.26 and the slow pool a ratio of 0.63. The middle figures show how a farmer's plow would homogenize the upper 20 cm, thus decreasing the observed $^{14}C/C$ ratio and carbon inventory for the surface soil. The bottom figures show how the $^{14}C/C$ ratio and carbon inventory change with a 25% loss of carbon, all from the fast-turnover pool.

REFERENCES AND NOTES

1. W. M. Post and L. K. Mann, in *Soils and the Greenhouse Effect*, A. F. Bowman, Ed. (Wiley, New York, 1990), pp. 401–407.
2. W. H. Schlesinger, *Biogeochemistry: An Analysis of Global Change* (Academic Press, New York, 1991), p. 135.
3. We estimated annual carbon fluxes using estimates of cultivated land area with time made by J. F. Richards [in *The Earth Transformed by Human Action: Global and Regional Changes in the Biosphere over the Past 300 Years*, B. L. Turner II *et al.*, Eds. (Cambridge Univ. Press, New York, 1990), pp. 163–178] and Schlesinger's (*2*) estimate that agricultural soil contains 180 GtC.
4. W. H. Schlesinger, in *The Changing Carbon Cycle—A Global Analysis* (Springer-Verlag, New York, 1986), pp. 194–200.
5. J. J. Schoenau, thesis, University of Saskatchewan (1988).
6. K. G. Harrison, W. S. Broecker, G. Bonani, *Global Biogeochem. Cycles* 7, 69 (1993).
7. B. J. O'Brien, *Radiocarbon* **28**, 358 (1986).
8. The data for uncultivated surface soils were listed in (*6*). New data were obtained for uncultivated surface soils in Lodi, Italy (collected in 1984, ^{14}C = 109% modern), Saskatoon, Saskatchewan, Canada (collected in 1985, ^{14}C = 122% modern), Konza Prairie, KS (collected in 1991, ^{14}C = 115% modern), and Durham, NC (collected in 1991, ^{14}C = 112% modern). The data for cultivated surface soils was obtained from: D. W. Anderson and E. A. Paul, *Soil Sci. Soc. Am. J.* **48**, 298 (1984); Y. A. Martel and E. A. Paul, *Can. J. Soil Sci.* **54**, 419 (1974); *Soil Sci. Soc. Am. Proc.* **38**, 501 (1974); H. W. Scharpenseel, P. Becker-Heidmann, H. U. Neue, K. Tsutsuke, *Sci. Total Environ.* **81**, 99 (1989); S. E. Trumbore, G. Bonani, W. Wolfi, in *Soils and the Greenhouse Effect*, A. F. Bouwman, Ed. (Wiley, New York, 1990), pp. 407–414; (*7*). Values for cultivated surface soils and published for the first time in this paper are from: Lodi, Italy (collected in 1984, ^{14}C = 103% modern), Konza Prairie, KS (collected in 1991, ^{14}C = 101% modern), and Saskatoon, Saskatchewan, Canada (collected in 1985, ^{14}C = 103% modern).

9. This research was supported by a grant from the Department of Energy and a National Aeronautics and Space Administration Global Change Fellowship. We thank two anonymous reviewers, whose critiques led to a greatly improved manuscript, and B. Zambella, who lent a discerning eye, careful hand, and timely resources. LDEO contribution S128.

10 May 1993; accepted 8 September 1993

Crustal Thickness on the Mid-Atlantic Ridge: Bull's-Eye Gravity Anomalies and Focused Accretion

Maya Tolstoy, Alistair J. Harding, John A. Orcutt

Spreading segments of the Mid-Atlantic Ridge show negative bull's-eye anomalies in the mantle Bouguer gravity field. Seismic refraction results from 33°S indicate that these anomalies can be accounted for by variations in crustal thickness along a segment. The crust is thicker in the center and thinner at the end of the spreading segment, and these changes are attributable to variations in the thickness of layer 3. The results show that accretion is focused at a slow-spreading ridge, that axial valley depth reflects the thickness of the underlying crust, and that along-axis density variations should be considered in the interpretation of gravity data.

The source of bull's-eye–shaped mantle Bouguer anomalies (MBAs) on the Mid-Atlantic Ridge (MAR) has been debated since they were first observed in 1988 (*1*). The MBA represents a simple correction of the observed gravity field for the effects of topography at both the sea floor and the Moho, assuming a constant crustal thickness (6 km) and constant densities [1030 kg/m^3 for seawater, 2730 kg/m^3 for crust, and 3330 kg/m^3 for mantle (*2*)]. Three possibilities for these anomalies have been proposed (*1*, *3*–*5*): (i) that they provide a window into the dynamics of the underlying mantle and are evidence of central upwelling plumes; (ii) that they may be attributable to along-axis crustal thickness variations; or (iii) a combination of the two. A seismic measurement can distinguish between these possibilities by providing an independent estimate of crustal thickness. Any of these explanations would indicate that magmatic accretion is focused (*3*) on the slow-spreading MAR. In focused accretion, the middles of segments are

Institute of Geophysics and Planetary Physics, Scripps Institution of Oceanography, University of California at San Diego, La Jolla, CA 92093.

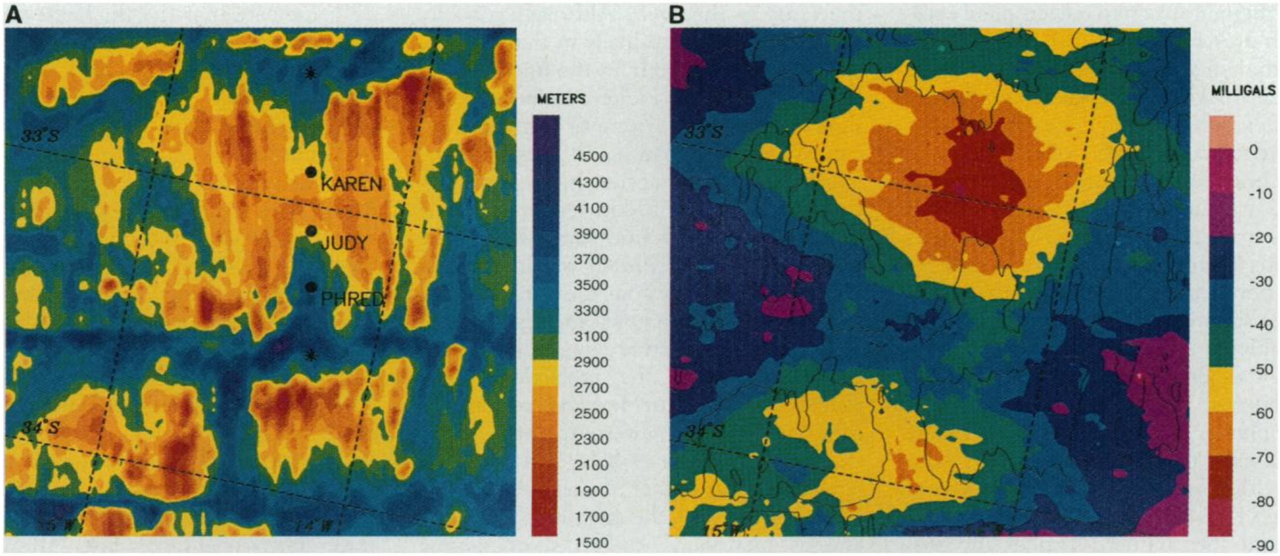

Fig. 1. (**A**) Bathymetry map of the 33°S segment of the southern MAR (*2*). Circles mark locations of OBSs and asterisks indicate the start and end points (bottom and top, respectively) of the shot line. (**B**) Mantle Bouguer anomaly for the 33°S segment, showing characteristic bull's-eye shape (*2*). A crustal thickness of 6 km was assumed. Black lines represent the 3-km bathymetry contour.

thought to have a robust magma supply and the ends are considered regions relatively starved of magma. Oceanic crust has two igneous layers, one extrusive (layer 2, basalts) and one intrusive-cumulative (layer 3, gabbros). Layer 1 corresponds to sediments, which are generally insignificant at the ridge crest. If the crustal thickness varies, whether the layers of the crust vary proportionally or independently is key to understanding the source of the variations. Here, we describe the results of a seismic refraction experiment along a segment with a large bull's-eye MBA.

The MAR segment at 33°S exhibits the largest observed bull's-eye MBA (~−90 mgal) (*1*). This pattern is associated with a central topographic high, where the median valley essentially disappears (6) (Fig. 1). The median valley then deepens toward the ends of the segment, assuming a morphology more typical of slow-spreading systems. A 109-km seismic refraction line was shot along the axis of the 33°S segment with the use of 54- and 27-kg explosive sources, and waves were detected with three ocean-bottom seismographs (OBSs) (Phred, Judy, and Karen).

The thickness of the ocean crust is indicated in the data by the time and range at which the high-amplitude reflections from the base of the crust (PmP) and arrivals with mantle velocities (8 km/s) are observed. The locations of these features are seen to increase in range from the seismographs as the center of the segment is approached (Fig. 2), which implies that the crust is thickening toward the center of the segment. Results from one-dimensional and two-dimensional models of the velocity structure required to fit the data are in good agreement and also imply that the crust is thick in the center of the segment and thins toward the end (Fig. 3). The thinning is clearly seen at the southern end of the segment; the data are too sparse at the northern end to accurately infer thinning. Model fits indicate that the overall change in crustal thickness appears to be primarily caused by variations in the thickness of layer 3 (Fig. 3). Consistent with the conclusions of earlier studies (*7–9*), the crustal section that contained velocities associated with layer 3 is apparently extremely thin or absent in the area of the fracture zone. The southern end of this segment is referred to as a second-order discontinuity (*10*). However, the similarity of the crustal structure to that of the first-order transform faults implies that this hierarchy relates primarily to the size of the offset of ridge segments and their surface expression, rather than to the crustal structure, and we refer to this offset simply as a fracture zone.

These calculations for seismic thickness can be compared with those predicted from the gravity anomaly. The gravity estimate is calculated by subtracting the effect of a passively upwelling mantle (*11*) (where the

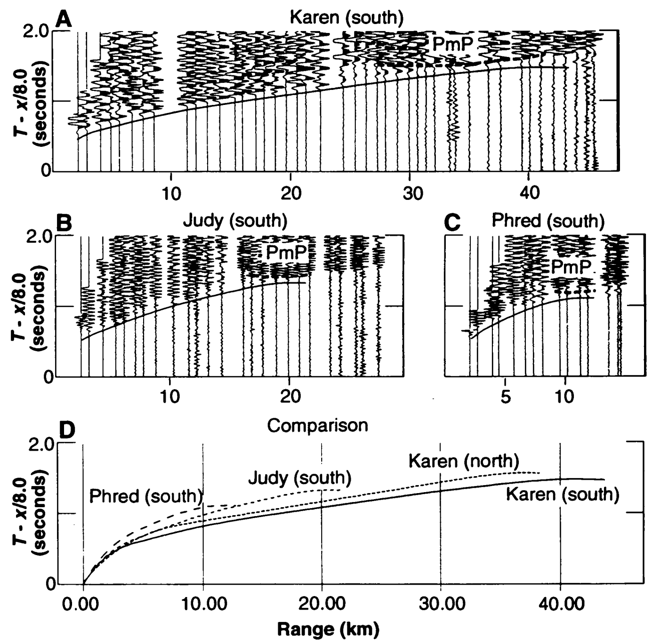

Fig. 2. (**A** through **C**) Travel time (T) versus range (X) plots of seismic data for OBSs Karen (A), Judy (B), and Phred (C). The solid lines are cubic spline fits to the initial *P*-wave arrival picks. The thick dashed line shows the area of high amplitude associated with the PmP arrival; the north-south labels indicate which side of the instrument the shots were on. The data are plotted with a reduction velocity of 8 km/s. Corrections for along-axis variations in topography were estimated by locating the least time entry point on the sea floor and subtracting the associated travel time to this entry point from the shot time (*30*). The data picks were then smoothed by fitting a cubic spline constrained to be monotonically decreasing in slope to permit a τ-p (where τ is delay time and p is the ray parameter) inversion for a smooth velocity-depth model (*31*). (**D**) A comparison of the cubic spline fits for four record sections on the 33°S segment.

mantle thermal structure reflects plate cooling with age) from the MBA and attributing all the remaining anomaly to variations in crustal thickness. This model essentially accounts for the west and east sides of the bull's-eye structure on the MBA, which are formed because of cooling, and therefore increase in density, of the mantle with distance from the ridge axis. The along-axis variations in crustal thickness then account for the north and south sides of the bull's-eye. The seismically observed variations in crustal thickness are more than adequate to produce the observed gravity anomaly (Fig. 3) without requiring the presence of a mantle plume. However, a mantle plume may still exist if the gravity signature associated with it is small [for example, a few milligals (*12*)].

Toward the southern end of the segment, the seismically determined thickness is less than predicted from the gravity data. For an isostatic relation, the variation in density required to account for this discrepancy is 260 kg/m^3. The observed disproportionate thinning of the higher density layer 3 indicates that crustal density is most likely not uniform. The thinning of layer 3 can account for over half of the density discrepancy estimated at the segment end. The remaining discrepancy may be attributed to the presence of upper crust with lowered densities in the area of the fracture zone. This conjecture is supported by data from the instrument nearest the fracture zone (Phred); here, upper crustal arrivals were delayed compared to arrivals at the central instruments (Fig. 2D). Densities may be lowered because of alteration and fracturing. Similar discrepancies between the seismically determined crustal thickness and gravity predictions in fracture zones have been observed elsewhere (*13*). The dual effects on the gravity signature of (i) increased central crustal density (reflecting a thick layer 3) and (ii) decreased density at the segment end (as a result of a thin layer 3 and low upper crustal densities) counteract each other. Together, they lead to an underestimation of the crustal thickness variation interpreted from the gravity data. Therefore, although gravity data provide a large-scale picture of crustal thickness variations, more detailed consideration requires seismic investigation because of lateral variations in crustal density. However, the accuracy of the gravity interpretation may be enhanced by considering the likely along-axis density variations of the crust.

A substantial layer 3 may not be recognized toward the fracture zone because it has been altered enough in that area that velocities have been lowered to those commonly associated with the extrusive layer 2. However, this would require extreme fracturing and alteration of the lower 2 km of the crust in this area. Although possible, this model seems less likely in that the area sampled is not directly in the fracture zone but only close to it. Earlier seismic work has shown that a broad zone of thinned crust extends out to 20 km on either side of the fracture zone and that the crust is extremely thin in a narrow, 10-km region spanning the axis of the fracture zone (*7–9*). The closest instrument (Phred) was located approximately 25 km from the center of the fracture zone and sampled the region 10 to 25 km from the fracture zone. It, therefore, primarily sampled the probable broader zone of thinned crust. For comparison, the Mesozoic crust in the western North Atlantic shows evidence of a layered cumulate sequence in the center of a segment, which disappears toward the fracture zone (*14*), and as mentioned earlier, most seismic work associated with fracture zones has identified little or no layer 3. There is no evidence, either from the topography (*6, 15*) or from earthquake studies (*16–18*), for ridge perpendicular faulting within segments on the MAR capable of producing along-axis crustal thickness variations of the magnitude we observed. The results at 33°S indicate that the thickness variations are associated with the accretion mechanism because layers 2 and 3 do not vary proportionally.

Our seismic results support the idea that accretion and upwelling are focused within individual segments of the slow-spreading MAR. The absence of a steady-state magma chamber on slow-spreading ridges (*16–22*) precludes significant along-axis migration of melt. Therefore, any focusing of the melt in upwelling mantle material on slow-spreading ridges would result in large variations in crustal thickness as observed in this experiment. In contrast, the more uniform crustal thickness of intermediate- to fast-spreading ridges is thought to reflect either an underlying two-dimensional mantle flow pattern (*23, 24*) or along-axis flow of magma redistributing a three-dimensional supply (*24, 25*).

These results identify a direct relation between crustal thickness and the morphology of the axial valley (Fig. 4). As the crust thickens, the axial valley shoals, and an axial high develops at maximum crustal thicknesses. There is no geochemical anomaly observed to indicate that this shoaling toward the center of the segment is

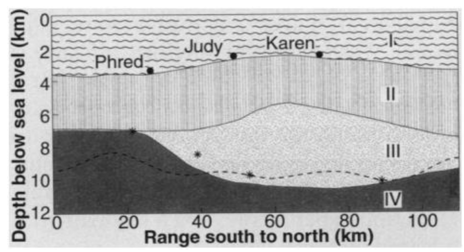

Fig. 3. Comparison of the two-dimensional seismic model and thickness predicted by gravity. Area I represents the ocean; area II is bounded by the surface topography (determined from the bathymetry data) and the 6.8 km/s velocity contour. Area II is interpreted to be crustal layer 2. Area III is bounded by the 6.8 km/s velocity contour and the base of the crust determined through two-dimensional seismic ray tracing; area III is interpreted to be crustal layer 3. Area IV is interpreted to be the mantle. The asterisks show the depth determined for the base of the crust from the one-dimensional seismic modeling; the dashed line is the crustal thickness predicted from gravity (*2*). One-dimensional models for the three instruments (Phred, Judy, and Karen) were produced iteratively with Wentzel-Kramers-Brillouin-Jeffreys (WKBJ) synthetic seismograms with the τ-p inversion as the starting model. The one-dimensional models were combined to produce an initial two-dimensional model. Through two-dimensional ray tracing (*30*), this model was adjusted to obtain a two-dimensional model consistent with the travel times. The two-dimensional model is well constrained only within the region of the asterisks. Based on the central data, the regions bounding this area are primarily schematic.

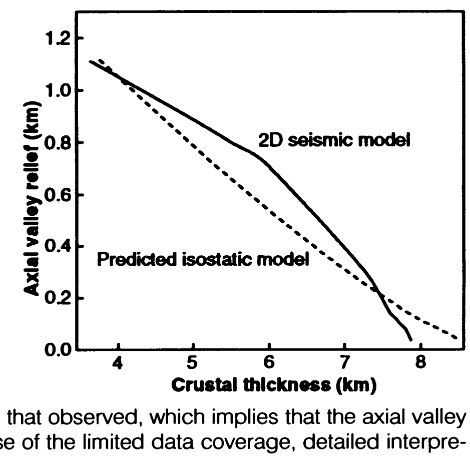

Fig. 4. Crustal thickness versus axial valley relief. The shallowest point of the valley is taken to be 0. The solid line is the relation of crustal thickness to axial valley relief as determined by the two-dimensional seismic model, using only the part of the model with good ray coverage (25 to 60 km) (Fig. 3). A linear relation of greater axial valley relief (depth) with a thinner crust would exist, assuming constant density, if the crust was isostatically compensated along the axis. The dashed line is the relation predicted if variations in axial valley relief were isostatically compensated, using a smoothly varying density of 2600 kg/m^3 for the deepest area and of 2800 kg/m^3 for the shallowest area and assuming a 3.5-km-thick crust at the deepest point in the valley. The curvature predicted is in the opposite direction to that observed, which implies that the axial valley relief is dynamically supported. However, because of the limited data coverage, detailed interpretation of the shape of the curve is unwarranted.

caused by the influence of nearby hot spots (26). Recent modeling (2, 27) predicts that at the slow-spreading rate [18 mm/year half spreading rate (28)] characteristic of the 33°S area, a transition in axial topography between forming or lacking an axial rift valley would correspond to crustal thicknesses of 7 to 8 km. This prediction is consistent with the seismically observed crustal thicknesses and topography in the 33°S area. This relation may be explained by variations in axial temperature consistent with focused accretion. If axial valley topography results from the stretching of a strong lithosphere, then a deeper axial valley may indicate the presence of a cool, brittle lithosphere, which would be associated with thin crust.

The results from 33°S indicate not only that crustal thickness variations can fully account for the observed MBA, but also that lateral variations of density within the crust are significant enough that they must be considered when gravity data are interpreted. It follows from these results that other bull's-eye MBAs inferred to exist along many ridge segments on the MAR may also be formed by along-axis crustal thickness variations. Such anomalies are also commonly associated with a shoaling of the axial valley similar to that observed in the 33°S area (4, 29). The regularity with which these characteristics are being observed suggests that they are a primary feature of the spreading mechanism operating along the slow-spreading MAR.

REFERENCES AND NOTES

1. B.-Y. Kuo and D. W. Forsyth, *Mar. Geophys. Res.* **10**, 205 (1988).
2. G. A. Neumann and D. W. Forsyth, *J. Geophys. Res.*, in press.
3. J. Lin, G. M. Purdy, H. Schouten, J.-C. Sempéré, C. Zervas, *Nature* **344**, 627 (1990).
4. D. K. Blackman and D. W. Forsyth, *J. Geophys. Res.* **96**, 11741 (1991).
5. J. Phipps Morgan, *Rev. Geophys. Suppl.* [*U.S. Nat. Rep. IUGG (1987–1990)*] **29**, 807 (1991).
6. P. J. Fox, N. R. Grindlay, K. C. MacDonald, *Mar. Geophys. Res.* **13**, 1 (1991).
7. R. S. Detrick and G. M. Purdy, *J. Geophys. Res.* **85**, 3759 (1980).
8. M. C. Sinha and K. E. Louden, *Geophys. J. R. Astron. Soc.* **75**, 713 (1983).
9. T. A. Minshull *et al.*, *J. Geophys. Res.* **96**, 9955 (1991).
10. N. R. Grindlay, P. J. Fox, K. C. MacDonald, *Mar. Geophys. Res.* **13**, 21 (1991).
11. J. Phipps Morgan and D. W. Forsyth, *J. Geophys. Res.* **93**, 2955 (1988).
12. M. Rabinowicz, S. Rouzo, J.-C. Sempéré, C. Rosemberg, *ibid.* **98**, 7851 (1993).
13. E. Morris and R. S. Detrick, *ibid.* **96**, 4355 (1991).
14. J. C. Mutter *et al.*, *Geology* **13**, 629 (1985).
15. J. A. Karson *et al.*, *Nature* **328**, 681 (1987).
16. R. C. Lilwal, *Geophys. J. R. Astron. Soc.* **51**, 357 (1977).
17. D. R. Toomey, S. C. Solomon, G. M. Purdy, *J. Geophys. Res.* **93**, 9093 (1988).
18. P. Y. Huang and S. C. Solomon, *ibid.*, p. 13445.
19. N. H. Sleep, *ibid.* **80**, 4037 (1975).
20. C. M. R. Fowler, *Geophys. J. R. Astron. Soc.* **47**, 459 (1976).
21. R. Batiza, W. G. Melson, T. O'Hearn, *Nature* **335**, 428 (1988).
22. R. S. Detrick, J. C. Mutter, P. Buhl, I. I. Kim, *ibid.* **347**, 61 (1990).
23. E. M. Parmentier and J. Phipps Morgan, *ibid.* **348**, 325 (1990).
24. J. Lin and J. Phipps Morgan, *J. Geophys. Res. Lett.* **19**, 13 (1992).
25. K. C. Macdonald *et al.*, *Nature* **335**, 217 (1988).
26. P. J. Michael *et al.*, in preparation.
27. J. Phipps Morgan and Y. J. Chen, *Nature*, in press.
28. S. Carbotte, S. M. Welch, K. C. Macdonald, *Mar. Geophys. Res.* **13**, 51 (1991).
29. J.-C. Sempéré, G. M. Purdy, H. Schouten, *Nature* **344**, 427 (1990).
30. D. W. Caress, M. S. Burnett, J. A. Orcutt, *J. Geophys. Res.* **97**, 9243 (1992).
31. P. B. Stark and R. L. Parker, *Geophys. J. R. Astron. Soc.* **89**, 997 (1987).

32. The seismic refraction line at 33°S was part of the Plume experiment, a multidisciplinary study that included bathymetry, seismics, gravity, magnetics, and dredging. We thank the officers, crew, and scientific complement of the R.V. *Thomas Washington* for their help in collecting these data. We also thank G. A. Neumann for providing the bathymetry and gravity data before its publication, D. Caress for his two-dimensional ray tracing program, P. Henkart for software, and D. K. Blackman, G. M. Kent, and J. Phipps Morgan for many helpful discussions. This work was supported by NSF.

28 June 1993; accepted 31 August 1993

The Manson Impact Structure: $^{40}Ar/^{39}Ar$ Age and Its Distal Impact Ejecta in the Pierre Shale in Southeastern South Dakota

G. A. Izett, W. A. Cobban, J. D. Obradovich, M. J. Kunk

The $^{40}Ar/^{39}Ar$ ages of a sanidine clast from a melt-matrix breccia of the Manson, Iowa, impact structure (MIS) indicate that the MIS formed 73.8 ± 0.3 million years ago (Ma) and is not coincident with the Cretaceous-Tertiary boundary (64.43 ± 0.05 Ma). The MIS sanidine is 9 million years older than $^{40}Ar/^{39}Ar$ age spectra of MIS shock-metamorphosed microcline and melt-matrix breccia interpreted earlier to be 64 to 65 Ma. Grains of shock-metamorphosed quartz, feldspar, and zircon were found in the Crow Creek Member (upper Campanian) at a biostratigraphic level constrained by radiometric ages in the Pierre Shale of South Dakota that are consistent with the $^{40}Ar/^{39}Ar$ age of 73.8 ± 0.3 Ma for MIS reported herein.

An iridium anomaly (*1*), shock-metamorphosed minerals (*2–4*), and relic tektites (*5*) in Cretaceous-Tertiary (K-T) boundary rocks provide evidence that at least one large extraterrestrial object struck the Earth 64.43 ± 0.05 Ma (*6*), probably in continental rocks in or near North America (*3, 7*). The rocks at two impact structures, Chicxulub on the Yucatan Peninsula and Manson in northwest Iowa, have been examined for evidence that might link them to the K-T impact. The Chicxulub structure (~200 km in diameter) has emerged as the leading candidate (*8, 9*), but the Manson structure (35 km in diameter) has also been proposed as a K-T boundary impact site because of its proximity to K-T boundary rocks containing large and abundant shocked minerals (*3, 7, 10*). Moreover, $^{40}Ar/^{39}Ar$ age spectra of MIS minerals and rocks, although complex and ambiguous, suggested to Kunk and colleagues (*11*) that the minerals and rocks underwent a shock-induced thermal event at 64 to 65 Ma, which is the time of the K-T boundary (64.4 Ma). Paleomagnetic data, however, imply that this interpretation is suspect. A high-temperature melt-matrix breccia layer in the MIS has normal remanent magnetization (*12*) and, if taken at face value, excludes the possibility that this structure formed at the K-T boundary, which is in reversely magnetized rocks in the upper part of magnetozone 29R (*13*). In addition, U-Pb ages of shock-metamorphosed zircons from the upper of two thin K-T boundary claystone beds of western North America indicate that their provenance was not Precambrian crystalline basement rocks in the Manson area or sedimentary rocks derived from such rocks (*4*).

In 1992, 12 holes were drilled to explore the MIS and to investigate further the isotopic age of the impact (*14*). The M-1 hole, on the flank of the central peak, penetrated a high-temperature, melt-matrix breccia layer 40 m thick (*15*). Examination of core from this rock revealed the presence of rare, chalky-white, microcrystalline feldspar (Fig. 1) with the optical properties of sanidine ($2V_x$ = 20° to 22°). The feldspar makes up centimeter-sized clasts in the melt matrix. Scanning electron microscope analysis showed that these clasts, which differ from the more common shocked and partially melted potassium feldspar (microcline) clasts, generally consist of spherulitic, radially bladed sanidine [K_2O (11.4 ± 0.7% w/w); $Or_{68}Ab_{31}An_1$] and trace amounts of

G. A. Izett, W. A. Cobban, J. D. Obradovich, U.S. Geological Survey, Denver, CO 80225.
M. J. Kunk, U.S. Geological Survey, Reston, VA 22092.